The Astrophysical Journal, 873:36 (7pp), 2019 March 1 https://doi.org/10.3847/1538-4357/ab03d4

The Role of Internal Photons on the Chemistry of the Circumstellar Envelopes of AGB Stars

M. Van de Sande[1] and T. J. Millar[2,3]
[1] Department of Physics and Astronomy, Institute of Astronomy, KU Leuven, Celestijnenlaan 200D, B-3001 Leuven, Belgium; marie.vandesande@kuleuven.be
[2] Astrophysics Research Centre, School of Mathematics and Physics, Queen's University Belfast, University Road, Belfast BT7 1NN, UK; tom.millar@qub.ac.uk
[3] Leiden Observatory, Leiden University, PO Box 9513, 2300 RA Leiden, The Netherlands
Received 2018 November 30; revised 2019 January 22; accepted 2019 January 30; published 2019 March 1

Abstract

Recent high spatial resolution observations of gas and dust in the circumstellar envelopes (CSEs) of AGB stars indicate morphologies much more complex than the smooth density distributions generated by spherically symmetric, constant mass-loss rates. In particular, the observation of spiral arcs and disks indicates the likely presence of a binary companion that in some cases gives rise to the UV photons detected by *Galaxy Evolution Explorer*. In this paper, we extend our recent model of the chemistry in a clumpy, porous CSE around an AGB star to include the influence of stellar blackbody photons on the CSE chemistry. Our results indicate that internal photons, in a clumpy, porous CSE, can alter chemistry within a few stellar radii and, for some molecules, alter abundances out to several hundred stellar radii. They further suggest that harder radiation from companion stars or accretion disks will have a substantial impact on chemistry in the dust formation zones and inner CSEs of AGB stars.

Key words: astrochemistry – circumstellar matter – stars: AGB and post-AGB

1. Introduction

Astrochemical studies of the the circumstellar envelopes (CSEs) of asymptotic giant branch (AGB) stars are of central importance in understanding macroscopic processes that are important in astronomy. These include the origin of interstellar dust, nucleosynthesis of the elements, the recycling of matter through mass loss, and the end points of stellar evolution. The CSEs are, in general, rich in molecular material, with close to 100 different molecules detected therein, as well as being efficient factories for the formation of the dust particles that populate the interstellar media of galaxies. They have long been known to contain large-scale density structures such as arcs and rings in both optical/near-IR (Mauron & Huggins 2000; Leão et al. 2006) and millimeter/submillimeter interferometric observations (Guélin et al. 1999; Dinh-V-Trung & Lim 2008; Agúndez et al. 2017). More recently, very high spatial resolution observations of both line and continuum emission have indicated the presence of structures such as spirals (Mauron & Huggins 2006; Decin et al. 2015; Quintana-Lacaci et al. 2016; Homan et al. 2018), disks (Kervella et al. 2014), and clumps, including small-scale structures close to the stellar photosphere (Khouri et al. 2016; Wittkowski et al. 2017; Decin et al. 2018).

The origin of such structures is still debated but there is evidence that binary companions may play an important role here (Decin et al. 2015; Quintana-Lacaci et al. 2017; Ramstedt et al. 2017) as well as in shaping the nonspherical morphologies of protoplanetary and planetary nebulae (De Marco 2009). Furthermore, recent *Galaxy Evolution Explorer* (*GALEX*) detections of UV radiation from AGB stars are argued to arise from sources that are either intrinsic, e.g., from chromospheres or pulsational shock waves (Montez et al. 2017), or extrinsic, e.g., from binary companions or accretion disks (Sahai et al. 2008, 2011, 2018). Ortiz et al. (2019) conclude that far-UV emission may be extrinsic but that further observations are required to draw a definite conclusion. The detection of CI in the O-rich AGB star omi Ceti has also been argued as due to an internal source of UV photons (Saberi et al. 2018).

In addition, the presence of "unexpected" molecules, such as hot H_2O in C-rich CSEs (Decin et al. 2010a; Neufeld et al. 2011) and CS, CN, and HCN in O-rich envelopes (Lindqvist et al. 1988; Bujarrabal et al. 1994), as well as the detection of species such as CH_3CN (Agúndez et al. 2015) and NaCN (Quintana-Lacaci et al. 2017) on angular scales of 1.5–3 arcsec, present a challenge for the traditional chemical kinetic models that incorporate a constant velocity and a constant mass-loss rate for the CSE structure.

Cordiner & Millar (2009) considered chemical models that included enhanced periods of mass loss to reproduce the observed, ring-like, molecular distributions in IRC+10216 with some success in that their additional shielding and increased shell density tended to restrict chemical evolution to these higher-density rings, but the model is unable to account for the presence of hot water deep in the CSE (Decin et al. 2010a). Nonthermal equilibrium processes driven by pulsation-induced shocks may provide sufficient H_2O (Cherchneff 2011, 2012). Another promising approach was introduced by Agúndez et al. (2010), who, on the basis of the clumpy structures seen in millimeter emission lines, presented a model that allowed a fraction of interstellar UV photons to penetrate deep into the CSE free from extinction due to circumstellar dust grains. This model was able to generate abundant, hot H_2O, in the inner CSE as well as perturb the chemistry in other ways. More recently, Van de Sande et al. (2018b) presented a more sophisticated porosity formalism that takes into account both an enhanced penetration of interstellar UV radiation, and the relative overdensity of clumps in the outflow. We describe its implementation in our model in Section 2.

Since clumped gas and dust appears to be present even at scales of the dust condensation radius in AGB stars (Agúndez et al. 2015; Decin et al. 2016, 2017, 2018; Kamiński et al. 2016, 2017; Quintana-Lacaci et al. 2017), it is natural to

consider whether or not the presence of an internal source of UV photons can drive a chemistry in the inner regions of the CSE, in regions opaque to interstellar UV. Furthermore, although AGB stars are cool and are not generally considered as sources of UV radiation that can affect CSE chemistry, we note that UV photons, such as those detected by *GALEX*, can penetrate the innermost CSE, particularly if it is clumpy. In this paper, we consider the simple case of UV photons generated by a blackbody at an effective temperature and use our porosity formalism to investigate the influence of UV emission from a cool AGB star on circumstellar chemistry, deferring a discussion of UV photons from a hotter companion to future work. This work is particularly timely in anticipation of the Cycle 6 ALMA Large Programme, ATOMIUM (2018.1.000659.L, PI: Decin), which will use Band 6 observations to study molecules in the dust formation zones of over 20 late-type stars.

2. Internal UV and the Porosity Formalism

The porosity formalism assumes that the CSE is composed of a stochastic ensemble of small-scale density enhancements or clumps, which take up a fraction $f_{\rm vol}$ of the total volume of the outflow, embedded in a rarefied interclump component, with a mean density relative to that of the smooth flow given by $f_{\rm ic}$. The density in the smooth flow is related to $f_{\rm vol}$ and $f_{\rm ic}$ by

$$\rho = (1 - f_{\rm vol})\rho_{\rm ic} + f_{\rm vol}\,\rho_{\rm cl}, \tag{1}$$

where we have suppressed the radial dependencies of the densities, and $\rho_{\rm cl}$ and $\rho_{\rm ic}$ are the clump and interclump densities, respectively. The ratio between the clump size $l(r)$ and $f_{\rm vol}$ represents the mean free path between the clumps, $h(r)$, a measure of the porosity of the outflow. Note that mass conservation within the clumps implies that both $l(r)$ and $h(r)$ are proportional to $r^{2/3}$. The specific clumpiness of the outflow is hence fully described by the parameters $f_{\rm vol}$, $f_{\rm ic}$, and l_*, the characteristic clump size at the stellar surface. The larger penetration of interstellar UV photons is taken into account by changing the optical depth of the outflow to an effective, clumpy, optical depth (Van de Sande et al. 2018b). Our model describes the chemical kinetic evolution of both the clump and interclump gas and calculates the fractional abundance of species X relative to H_2 as a function of radius via

$$y_{\rm X} = y_{\rm cl,X} + f_{\rm ic}(1 - f_{\rm vol})(y_{\rm ic,X} - y_{\rm cl,X}). \tag{2}$$

As a first approximation we have used blackbody radiation to determine the internal UV fluxes. We have considered whether stellar atmosphere models can provide a more accurate estimate but find that the Kurucz,[4] MARCS,[5] and PHOENIX[6] models have either temperatures or surface gravities that are too large than those appropriate for well-observed low-to-intermediate mass AGB stars such as CW Leo and R Dor (Castelli & Kurucz 2003; Gustafsson et al. 2008; Husser et al. 2013). Calculated values of log g are −1.4 for IRC+10216 and −1.17 for R Dor, both smaller than those offered by stellar atmosphere models. Figure 1 shows the blackbody photon flux at 2.5×10^{15} cm (50 R_* for IRC +10216) for the wavelength range 912–2100 Å, approximately 6–13.6 eV. Although there are negligible photons at the shortest wavelengths, the figure shows that the flux increases rapidly at longer wavelengths. We have calculated the photon flux, $F_{*,\rm sc}(\lambda)$, at a fiducial radius, $R_{\rm sc} = 50\,R_*$, and used this to derive the unshielded photorate coefficients with cross sections taken from the Leiden Observatory Database[7] (Heays et al. 2017) as

$$\alpha_{0,\rm sc}^{\rm IP} = \int F_{*,\rm sc}(\lambda)\sigma(\lambda)d\lambda. \tag{3}$$

This data set covers over 120 photoreaction channels in our network. To these, we have used a mixture of laboratory measurements and theoretical calculations on electron affinities (EAs) to estimate the photodetachment rates of around 25 anions (Arnold et al. 1991; Blanksby et al. 2001; Yen et al. 2010; Best et al. 2011; Kumar et al. 2013; Senent & Hochlaf 2013) with cross sections determined from the formula given by Millar et al. (2007):

$$\sigma = \sigma_\infty(1 - {\rm EA}/E)^{0.5}, \tag{4}$$

where σ_∞ is the asymptotic cross section at high energy and E is the photon energy. We note that anions do not influence the chemistry of the inner CSE significantly as they undergo rapid photodetachement due to their low EA.

For species for which cross sections are not available, we have scaled the interstellar unshielded rate by the ratio of the integrated fluxes of stellar to interstellar photons (integrated over 6–13.6 eV), a common approach in astrochemical modeling:

$$\alpha_0^{\rm IP} = \left(\frac{G_*}{G_{\rm IS}}\right)\alpha_0^{\rm IS}, \tag{5}$$

where

$$G = \int_{2068\ \text{Å}}^{912\ \text{Å}} F(\lambda)d\lambda. \tag{6}$$

We note, however, that this approach can significantly overestimate the photoionization rates for molecules as their ionization potentials generally fall at higher energies, where the flux of stellar UV photons is negligible, than their bond dissociation energies. For these species, we have therefore used a scaling factor, determined from comparing photoionization rates calculated from (exact) atomic cross sections (Equation (3)) with those from the integrated approach (Equation (5)) to reduce their calculated rates to insignificant values. In total, we include 436 photochannels due to internal photons.

At every radial distance r, we calculate the effective dust extinction in the porosity formalism, $A_{\rm V}^{\rm eff}$, in terms of the optical depth for a uniform outflow, $A_{\rm V}$. The equations for both a one-component model, where the interclump medium is void, and a two-component model, where mass is distributed in both a clump and interclump medium, are given in Appendix C of Van de Sande et al. (2018b). The internal photon flux is diluted geometrically and extinguished by dust. For the dust extinction experienced by internal photons, the dust condensation radius is set at 1.9 R_*, or at a temperature close to 1500 K.

As an example of this procedure, Figure 2 shows the photodissociation rate of SO as a function of radius for both internal and external photons for blackbody temperatures of 2330 K (blue) and 2600 K (orange) and a mass-loss rate of $10^{-7}\ M_\odot\ {\rm yr}^{-1}$. Solid curves correspond to a smooth outflow,

[4] http://kurucz.harvard.edu/grids.html
[5] http://marcs.astro.uu.se/
[6] http://osubdd.ens-lyon.fr/phoenix/
[7] http://www.strw.leidenuniv.nl/~ewine/photo

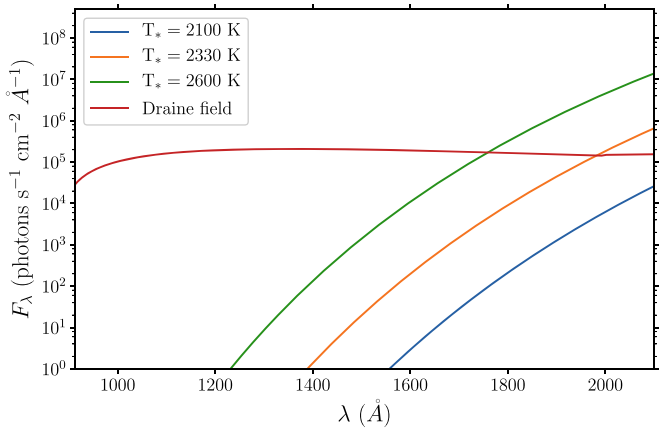

Figure 1. Blackbody flux at a distance of $50\,R_*$ for a stellar radius of 5×10^{13} cm for temperatures of 2100 K, 2330 K (equivalent to IRC+10216), and 2600 K.

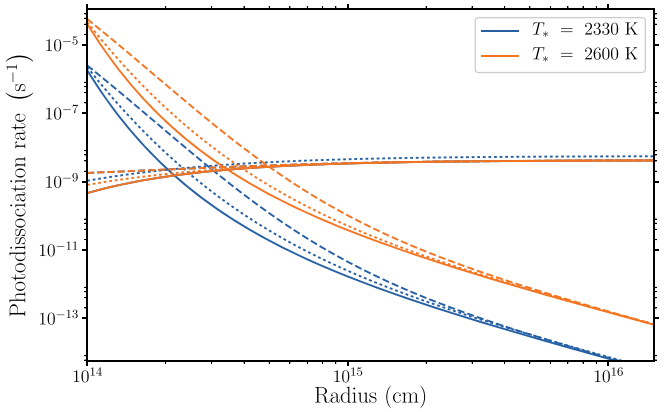

Figure 2. Internal and external UV photodissociation rates of SO are plotted as a function of radius for a mass-loss rate of $10^{-7}\,M_\odot\,\mathrm{yr}^{-1}$ for effective stellar temperatures of 2330 K (blue; equivalent to IRC+10216) and 2600 K (orange). Solid curves represent a smooth outflow, dashed curves a one-component outflow with $f_{\rm vol} = 0.1$ and $l_* = 10^{13}$ cm, and dotted curves a two-component outflow with $f_{\rm vol} = 0.1$, $f_{\rm ic} = 0.5$, and $l_* = 10^{13}$ cm.

dashed curves to a one-component porosity model (effectively void interclump component), with $f_{\rm vol} = 0.1$ and $l_* = 10^{13}$ cm, and dotted curves to a two-component model with $f_{\rm ic} = 0.5$, i.e., equal mass in the clump and interclump gas and the same $f_{\rm vol}$ and l_* as the one-component model. The importance of internal photons to direct photodissociation of SO increases at the hotter temperature and dominates the interstellar rate only inside 3–6 $\times$ 10^{14} cm. Species with low bond energies can have rate coefficients due to internal photons substantially larger than their interstellar values, whereas those with strong bonds, such as CO and N_2, are not affected by the presence of these internal photons.

3. Results

We have made a set of calculations for a range of mass-loss rates, 10^{-5}–10^{-7} $M_\odot\,\mathrm{yr}^{-1}$, and for both C-rich and O-rich AGB stars, with initial abundances given in Agúndez et al. (2010) and using the chemical model described by McElroy et al. (2013), publicly available through the UMIST Database for Astrochemistry website,[8] adapted by Van de Sande et al. (2018b) to include a clumpy outflow. The calculations have been performed for a smooth outflow, a one-component outflow with $f_{\rm vol} = 0.1$ and $l_* = 10^{13}$ cm, and a two-component with $f_{\rm ic} = 0.5$, $f_{\rm vol} = 0.1$, and $l_* = 10^{13}$ cm. We choose some representative species to discuss both the direct and indirect effects of internal UV on abundance distributions. The selection of these species is based on (i) their observability, (ii) their formation and destruction pathways being sensitive to the presence of internal photons, and (iii) some being "unexpected," e.g., H_2O in C-rich and HCN and CS in O-rich CSEs. We concentrate here on the results at the two lower mass-loss rates and for the smooth and one-component clumpy outflows only. At the highest mass-loss rate, the effects of internal photons are less important because of the significantly higher extinction in this case (see Van de Sande et al. 2018b). Similarly, the effects of internal photons in the two-component model are less pronounced due to its higher effective extinction than in the one-component model.

3.1. Carbon-rich Outflows

Figure 3 shows the radial fractional abundances and Table 1 the radial column densities of CH_4, SO, NH_3, and H_2O for the C-rich case for 2100 K (blue), 2330 K (orange), and 2600 K (green). Solid curves refer to a smooth outflow without internal photons, dashed curves to a smooth outflow with internal photons, and dotted curves to a clumpy, one-component outflow with internal photons.

The CH_4 abundance in the C-rich outflow can change by up to five orders of magnitude for r less than 4×10^{15} cm due to a combination of internal photons and clumpiness (Figure 3(A)). Internal photons liberate carbon from the C-bearing parent species HCN and CS, with a larger increase in abundance for the higher stellar temperature. Fast neutral–neutral reactions involving H_2 effectively hydrogenate carbon to form CH_4, transferring the increase in C abundance to CH_4. The CH_4 radial behavior changes for a clumpy outflow, because despite the larger C abundance due to photodissociation by interstellar photons of HCN and CS, the increased penetration of the internal photons now destroys the newly formed carbon hydrides. The increased destruction of carbon hydrides by internal photons causes the decrease in CH_4 abundance when including internal photons at $\dot{M} = 10^{-7}\,M_\odot\,\mathrm{yr}^{-1}$ (Figure 3(B)). For a clumpy outflow, the larger C abundance in the inner regions compensates this effect, albeit only close to the star for the higher stellar temperature. At lower temperatures the dust extinction is sufficiently large for the carbon hydrides to form, leading to an overall larger CH_4 abundance.

For SO, the two main formation reactions are O + HS → SO + H and OH + S → SO + H. Which reaction dominates depends on the relative abundances of the reactants. Photodissociation of the parent species SiS by internal photons liberates S close to the star. Hydrogenation of S leads to the formation of HS, increasing its abundance in the innermost region as well. The SO radial behavior hence roughly follows that of HS. For a higher stellar temperature and a clumpy or lower mass-loss rate outflow, the HS abundance decreases rapidly due to reactions with H. In such outflows, H is more abundantly present due to internal photons. In this case, the OH + S reaction then takes over and the SO radial behavior follows that of OH. OH is formed through the hydrogenation of O, whose abundance increases slightly in the inner region due to photodissociation of the parent species SiO. CO is not affected by internal photons due to its small photodissociation rate. In

[8] www.udfa.net

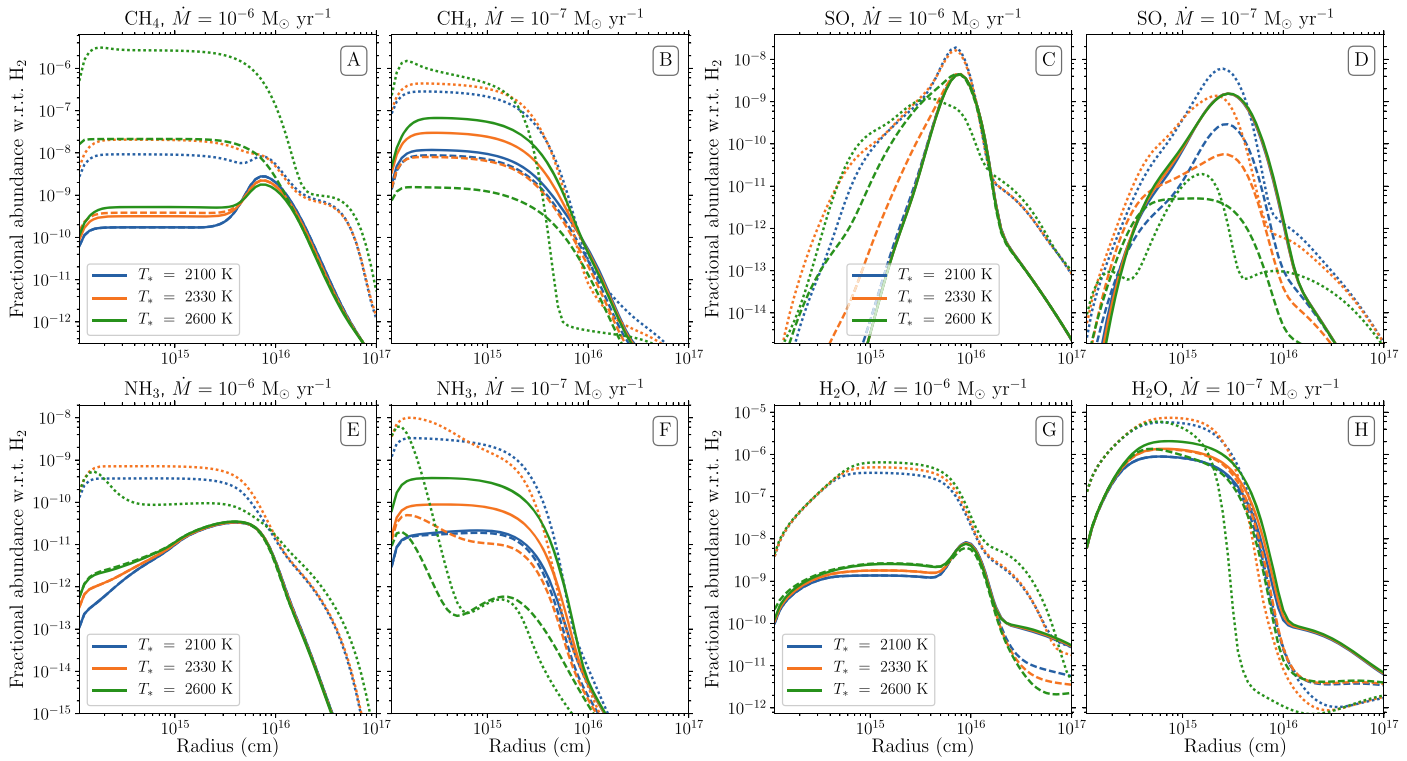

Figure 3. Radial fractional abundance of CH_4, SO, NH_3, and H_2O for 2100 K (blue), 2330 K (orange), and 2600 K (green) in the C-rich case. Solid curves refer to a smooth outflow without internal photons, dashed curves to a smooth outflow with internal photons, and dotted curves to a clumpy, one-component outflow with internal photons.

Table 1

Column Density (cm^{-2}) of CH_4, SO, NH_3, and H_2O in a C-rich Outflow for a Smooth Outflow without and with Internal Photons and a One-component Clumpy Outflow ($f_{vol} = 0.1$ and $l_* = 10^{13}$ cm) with Internal Photons

$\dot{M}$	T_*	Smooth, no IP		Smooth, with IP		Clumpy, with IP	
		CH_4	SO	CH_4	SO	CH_4	SO
$10^{-5} M_\odot$ yr^{-1}	2100 K	1.56e+13	6.60e+11	1.56e+13	6.60e+11	2.02e+13	1.85e+12
	2330 K	2.32e+13	6.59e+11	2.32e+13	6.59e+11	1.34e+14	3.94e+12
	2600 K	3.34e+13	6.57e+11	3.34e+13	6.57e+11	1.43e+16	6.54e+13
$10^{-6} M_\odot$ yr^{-1}	2100 K	1.28e+12	2.69e+11	1.28e+12	2.71e+11	5.46e+13	1.38e+12
	2330 K	2.02e+12	2.66e+11	2.48e+12	3.17e+11	1.15e+14	1.30e+12
	2600 K	3.01e+12	2.63e+11	1.44e+14	5.11e+11	1.67e+16	4.35e+11
$10^{-7} M_\odot$ yr^{-1}	2100 K	6.04e+12	4.28e+10	4.56e+12	7.94e+09	1.56e+14	1.67e+11
	2330 K	1.45e+13	4.33e+10	4.28e+12	3.63e+09	2.32e+14	6.38e+10
	2600 K	2.99e+13	4.40e+10	9.25e+11	9.02e+08	6.00e+14	9.67e+08
		NH_3	H_2O	NH_3	H_2O	NH_3	H_2O
$10^{-5} M_\odot$ yr^{-1}	2100 K	5.06e+11	6.03e+13	5.06e+11	6.03e+13	6.57e+11	9.44e+13
	2330 K	5.65e+11	7.00e+13	5.65e+11	7.00e+13	7.56e+11	8.31e+14
	2600 K	6.27e+11	8.15e+13	6.27e+11	8.15e+13	8.48e+11	1.74e+14
$10^{-6} M_\odot$ yr^{-1}	2100 K	2.29e+10	5.54e+12	2.29e+10	5.54e+12	2.24e+12	8.08e+14
	2330 K	2.67e+10	6.54e+12	2.67e+10	6.53e+12	4.10e+12	9.63e+14
	2600 K	3.25e+10	7.91e+12	3.35e+10	8.50e+12	1.80e+12	1.13e+15
$10^{-7} M_\odot$ yr^{-1}	2100 K	1.04e+10	2.43e+14	9.51e+09	2.42e+14	1.84e+12	1.56e+15
	2330 K	4.72e+10	3.36e+14	2.04e+10	3.29e+14	4.51e+12	1.79e+15
	2600 K	1.95e+11	4.59e+14	5.40e+09	3.21e+14	1.52e+12	1.46e+15

Note. The corresponding abundance profiles are shown in Figure 3.

low mass-loss rate and high stellar temperature outflows, OH is formed in greater abundances close to the star thanks to the photodissociation of H_2O by internal and, for clumpy outflows, interstellar photons. The extent of its molecular shell is, however, limited due to the photodissociation of H_2O itself, which is reflected in the SO abundance profile.

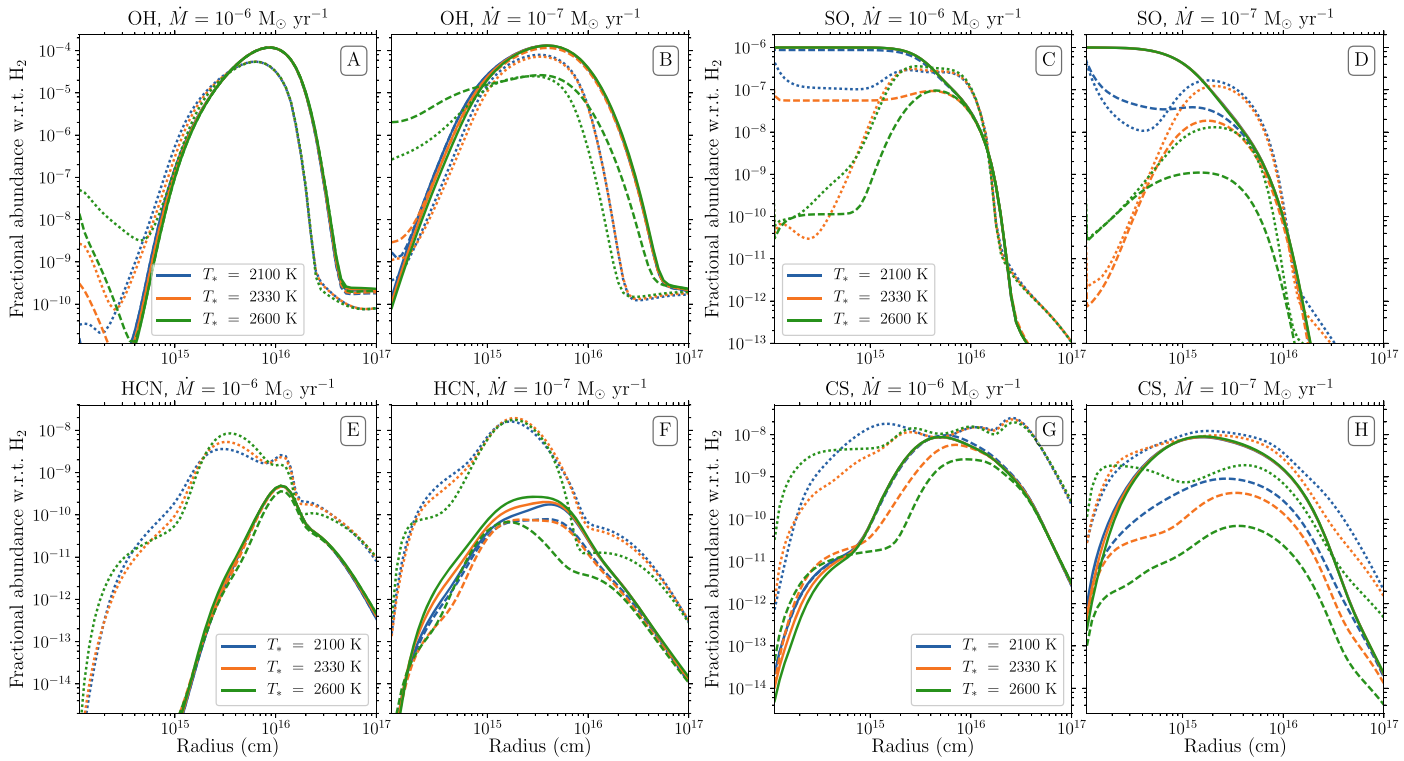

Figure 4. Radial fractional abundance of OH, SO, HCN, and CS for 2100 K (blue), 2330 K (orange), and 2600 K (green) in the O-rich case. Solid curves refer to a smooth outflow without internal photons, dashed curves to a smooth outflow with internal photons, and dotted curves to a clumpy, one-component outflow with internal photons.

For NH_3, internal photons affect the inner regions only for outflows with $\dot{M} = 10^{-6}\,M_\odot\,\mathrm{yr}^{-1}$ but a more extended region for lower mass-loss rate outflows. Smooth outflows with $\dot{M} = 10^{-6}\ M_\odot\ \mathrm{yr}^{-1}$ have abundances that are essentially unaffected by the inclusion of internal photons but that, when both clumps and internal photons are present, increase by two to three orders of magnitude at r smaller than 10^{15} cm and are always larger than the smooth models at all radii (Figure 3 (E)). In the clumpy outflow, NH_3 is formed at $r \leqslant 10^{15}$ cm through the reactions $H_2 + N \rightarrow NH + H$ and $O + HCN \rightarrow NH + CO$, followed by H atom abstraction reactions with H_2. Here O atoms are liberated through the photodissociation by internal photons of the parent species SiO. In the higher-temperature models, the NH_3 abundance is lower due to the loss of O atoms through fast reaction with H_2. The behavior of NH_3 in clumpy outflows and outflows with $\dot{M} = 10^{-7}\ M_\odot\ \mathrm{yr}^{-1}$ is similar to that of CH_4, although its absolute abundance is generally lower due to its larger internal photodissociation rate.

H_2O is only affected by internal photons for lower mass-loss rate outflows (Figure 3(H)). The increase seen in clumpy outflows is due to the clumpiness of the outflow, rather than the presence of internal photons. The very small increase for $T_* = 2600$ K is caused by the larger O abundance close to the star. For outflows with high stellar temperatures, OH is photodissociated close to the star by internal photons, leading to a decrease in H_2O abundance closer to the star. This decline in abundance closer to the star also holds for the clumpy outflows with a high stellar temperature compared to the clumpy outflow without internal photons.

3.2. Oxygen-rich Outflows

Figure 4 presents the abundances and Table 2 the radial column densities of OH, SO, HCN, and NH_3 in the case of an O-rich outflow. For the higher mass-loss rate of $10^{-6}\ M_\odot\,\mathrm{yr}^{-1}$, the production of OH is enhanced by internal photons inside 10^{15} cm due to the photodissociation of the parent H_2O, although we note that only around 1% of water is destroyed in this region. At the lowest mass-loss rate, extinction is reduced and the higher UV flux at $T_* = 2600$ K results in the efficient photodissociation of OH so that its abundance is much reduced over the range 10^{15}–10^{17} cm. Despite its larger inner wind abundance, the radial profile of clumpy, lower mass-loss rate outflow follows that of H_2O as well: due to the large porosity of the outflow, the molecular envelope of H_2O only reaches to $\sim 10^{15}$ cm and gives rise to the large OH abundance inside 3–4 $\times\ 10^{14}$ cm.

SO is included as a parent species in the O-rich outflow. Internal photons photodissociate SO in the innermost region, leading to a decrease in its abundance of up to five orders of magnitude (Figure 4(D)). Its destruction is larger for a higher stellar temperature. In the case of a clumpy or lower $\dot{M}$ outflow, the SO abundance close to the star is, however, larger for higher T_*. This is due to the larger OH abundance in this region for these outflows, which replenishes the SO abundance through the reaction $OH + S \rightarrow SO + H$.

The large increase in HCN abundance seen for clumpy outflows (Figure 4(E)), is mainly due to the clumpiness of the outflow rather than due to internal photons. For r smaller than 10^{15} cm, the decrease in abundance is due to photodissociation by internal photons. Around 10^{15} cm, its main production reaction shifts from $H_2 + CN \rightarrow HCN + H$ to $N + CH_2 \rightarrow HCN + H$. The CH_2 abundance is smaller for higher stellar

Table 2
Column Density (cm^{-2}) of OH, SO, HCN, and CS in an O-rich Outflow for a Smooth Outflow without and with Internal Photons and a One-component Clumpy Outflow ($f_{vol} = 0.1$ and $l_* = 10^{13}$ cm) with Internal Photons

$\dot{M}$	T_*	Smooth, no IP		Smooth, with IP		Clumpy, with IP	
		OH	SO	OH	SO	OH	SO
$10^{-5} M_\odot$ yr^{-1}	2100 K	2.54e+16	6.69e+16	2.54e+16	6.69e+16	2.33e+16	2.42e+16
	2330 K	2.55e+16	6.69e+16	2.55e+16	6.69e+16	2.35e+16	1.23e+14
	2600 K	2.53e+16	6.69e+16	2.53e+16	6.69e+16	2.29e+16	2.30e+14
$10^{-6} M_\odot$ yr^{-1}	2100 K	1.62e+16	6.49e+15	1.62e+16	5.68e+15	1.14e+16	1.13e+15
	2330 K	1.62e+16	6.49e+15	1.62e+16	3.87e+14	1.09e+16	1.27e+14
	2600 K	1.61e+16	6.49e+15	1.61e+16	2.23e+13	1.04e+16	1.31e+14
$10^{-7} M_\odot$ yr^{-1}	2100 K	6.11e+15	5.71e+14	6.06e+15	7.30e+13	3.55e+15	5.38e+13
	2330 K	5.85e+15	5.71e+14	5.15e+15	1.22e+12	3.00e+15	6.31e+12
	2600 K	5.56e+15	5.71e+14	4.21e+15	1.87e+11	2.10e+15	9.57e+11
		HCN	CS	HCN	CS	HCN	CS
$10^{-5} M_\odot$ yr^{-1}	2100 K	4.97e+10	5.03e+12	4.97e+10	5.03e+12	5.45e+11	2.18e+13
	2330 K	5.01e+10	4.16e+12	5.01e+10	4.16e+12	5.45e+11	1.28e+13
	2600 K	5.31e+10	4.67e+12	5.31e+10	4.67e+12	5.29e+11	3.77e+13
$10^{-6} M_\odot$ yr^{-1}	2100 K	2.48e+10	2.14e+12	2.49e+10	2.21e+12	1.35e+12	2.06e+13
	2330 K	2.52e+10	2.14e+12	2.37e+10	1.03e+12	1.55e+12	8.86e+12
	2600 K	2.57e+10	2.14e+12	1.76e+10	4.16e+11	2.01e+12	2.02e+13
$10^{-7} M_\odot$ yr^{-1}	2100 K	7.77e+09	1.08e+12	5.04e+09	9.18e+10	9.84e+11	1.95e+12
	2330 K	1.04e+10	1.07e+12	4.70e+09	3.02e+10	1.01e+12	1.92e+12
	2600 K	1.50e+10	1.05e+12	4.38e+09	4.63e+09	8.82e+11	8.86e+11

Note. The corresponding abundance profiles are shown in Figure 4.

temperatures, as internal photons more readily destroy hydrogenated carbon, leading to a decline in the peak HCN abundance, which is larger for lower mass-loss rate outflows.

As for HCN, the large increase in the CS abundance for the clumpy outflows is again mainly the result of clumpiness rather than internal photons. For the lower mass-loss rate outflows, the peak CS abundance decreases up to two orders of magnitude when including internal photons in a clumpy or smooth outflow. At radial distances less than 10^{15} cm, the main reaction forming CS is $HCS^+ + e^- \rightarrow CS + H$, where HCS^+ is mostly formed via $CH_3^+ + S \rightarrow HCS^+ + H_2$. Including internal photons leads to a larger S abundance close to the star, due to the photodissociation of the parent species H_2S. This then leads to a larger HCS^+ abundance, and therefore CS abundance. In clumpy outflows with 10^{-7} $M_\odot$ yr^{-1}, the CS abundance decreases before 10^{15} cm (Figure 4(H)). This is linked to the increased O abundance close to the star when including internal photons, destroying CS via the reaction $O + CS \rightarrow S + CO$. Beyond 10^{15} cm, the main reaction forming CS shifts to $C + SO \rightarrow CS + O$. The influence of internal photons on the SO abundance is hence propagated to the CS abundance profile, causing a decrease in peak abundance of up to two orders of magnitude.

4. Discussion

Our calculations show that the internal UV photons in combination with a clumpy outflow can have a significant effect on the chemistry and radial distributions of specific molecules in both C-rich and O-rich AGB envelopes, in particular, forming the "unexpected" molecules seen in these envelopes (see Section 1).

For the largest mass-loss rate considered, 10^{-5} $M_\odot$ yr^{-1}, we find that the dust extinction renders these photons unimportant for the blackbody temperatures we have assumed here. Inner photons hence cannot account for the observed column density of NH_3 of the high mass-loss rate C-rich AGB star IRC+10216 (Schmidt et al. 2016), one of its "unexpected" species. For lower mass-loss rates, we find our clumpy models can give rise to significantly enhanced abundances of several species in the inner CSE, around 10^{15} cm. For example, in our C-rich calculations, we find water abundances on the order of (3–60) $\times$ 10^{-7}, consistent with the abundances found by Lombaert et al. (2016) in their study of C-rich AGB stars, while the H_2O column density is enhanced by one to two orders of magnitude for effective temperatures of 2100 and 2330 K (Table 1). For O-rich outflows, we find that HCN reaches peak abundances of around 10^{-8}, less than the peak abundances of around 5×10^{-7} observed in IK Tau (Decin et al. 2010b) and R Dor (Van de Sande et al. 2018a). Although these peak abundances fall below those observed, we find that the HCN column densities are much enhanced, by around one to two orders of magnitude when internal photons are included (Table 2), even for mass-loss rates as large as 10^{-5} $M_\odot$ yr^{-1}.

Our models do have limitations. In addition to the uncertainty associated with calculating the photodissociation rates of species for which no wavelength-dependent cross sections are available, much of our gas-phase chemistry in the inner envelope occurs at high temperatures where two-body reactions are less well studied and hence may raise issues of completeness of chemistry. Although not shown here, two-component clumpy models generally show smaller effects of UV photons than the one-component model presented here. Such models have higher effective extinction as the interclump medium is not void and would diminish the effects of internal photons. Additionally, as

noted in Section 1, many AGB stars may contain binary companions. The presence of harder radiation fields from a hot binary or associated accretion disk might also be expected to change results appreciably. Finally, we have used a blackbody spectrum to calculate the UV photons emitted by the AGB star due to the limited ranges of stellar temperatures and surface gravities covered by stellar atmosphere models. Blackbody spectra, however, do not take into account the effects of molecular bands on the emitted UV spectrum and introduce a potentially significant uncertainty into our results.

5. Conclusions

We have presented the first model calculations that include the chemical effects of internal UV photons, here assumed to be blackbody radiation from cool AGB stars using the porosity formalism introduced by Van de Sande et al. (2018b) and the CSE chemistry code from McElroy et al. (2013). For the radiation fields used here, we find that internal photons are essentially unimportant at $10^{-5}\ M_{\odot}\,\mathrm{yr}^{-1}$ due to the large value of dust extinction.

Our results show that at lower mass-loss rates, for a clumpy circumstellar medium close to the photosphere, as is observed for several AGB stars, these UV photons are capable of influencing the chemistry that occurs deep in the CSE. These effects are more significant the larger the effective temperature and, in general, the lower the mass-loss rate. The distribution of molecules can be altered either directly through enhanced photodissociation rates or indirectly through changes to the abundances of other species involved in their formation or destruction. We find that the radial distribution of the fractional abundance of H_2O in C-rich outflows is significantly enhanced in the inner envelope while its column density and that of HCN in O-rich outflows can increase by 1–2 orders of magnitude when internal photons and clumps are included in models.

In future work, we shall consider the influence of harder radiation fields, but it is clear that chemical kinetic models of the inner winds of AGB stars, including those of dust formation and shock chemistry following stellar pulsations, should include the photochemistry driven by these internal photons.

We thank the anonymous referee for providing useful comments that helped improve this article. T.J.M. is grateful to the STFC for support through grant ST/P000321/1 and for the hospitality of Leiden Observatory where much of this work was carried out. M.V.d.S. acknowledges support from the Research Foundation—Flanders through grant 12X6419N.

ORCID iDs

M. Van de Sande https://orcid.org/0000-0002-0786-7307
T. J. Millar https://orcid.org/0000-0001-5178-3656

References

Agúndez, M., Cernicharo, J., & Guélin, M. 2010, ApJL, 724, L133
Agúndez, M., Cernicharo, J., Quintana-Lacaci, G., et al. 2015, ApJ, 814, 143
Agúndez, M., Cernicharo, J., Quintana-Lacaci, G., et al. 2017, A&A, 601, A4
Arnold, D. W., Bradforth, S. E., Kitsopoulos, T. N., & Neumark, D. M. 1991, JChPh, 95, 8753
Best, T., Otto, R., Trippel, S., et al. 2011, ApJ, 742, 63
Blanksby, S. J., McAnoy, A. M., Dua, S., & Bowie, J. H. 2001, MNRAS, 328, 89
Bujarrabal, V., Fuente, A., & Omont, A. 1994, A&A, 285, 247
Castelli, F., & Kurucz, R. L. 2003, in IAU Symp. 210, Modelling of Stellar Atmospheres, ed. N. Piskunov, W. W. Weiss, & D. F. Gray (San Francisco, CA: ASP), A20
Cherchneff, I. 2011, A&A, 526, L11
Cherchneff, I. 2012, A&A, 545, A12
Cordiner, M. A., & Millar, T. J. 2009, ApJ, 697, 68
De Marco, O. 2009, PASP, 121, 316
Decin, L., Agúndez, M., Barlow, M. J., et al. 2010a, Natur, 467, 64
Decin, L., Danilovich, T., Gobrecht, D., et al. 2018, ApJ, 855, 113
Decin, L., De Beck, E., Brünken, S., et al. 2010b, A&A, 516, A69
Decin, L., Richards, A. M. S., Millar, T. J., et al. 2016, A&A, 592, A76
Decin, L., Richards, A. M. S., Neufeld, D., et al. 2015, A&A, 574, A5
Decin, L., Richards, A. M. S., Waters, L. B. F. M., et al. 2017, A&A, 608, A55
Dinh-V-Trung, & Lim, J. 2008, ApJ, 678, 303
Guélin, M., Neininger, N., Lucas, R., & Cernicharo, J. 1999, in The Physics and Chemistry of the Interstellar Medium, ed. V. Ossenkopf, J. Stutzki, & G. Winnewisser (Herdecke: GCA-Verlag), 326
Gustafsson, B., Edvardsson, B., Eriksson, K., et al. 2008, A&A, 486, 951
Heays, A. N., Bosman, A. D., & van Dishoeck, E. F. 2017, A&A, 602, A105
Homan, W., Richards, A., Decin, L., de Koter, A., & Kervella, P. 2018, A&A, 616, A34
Husser, T. O., Wende-von Berg, S., Dreizler, S., et al. 2013, A&A, 553, A6
Kamiński, T., Müller, H. S. P., Schmidt, M. R., et al. 2017, A&A, 599, A59
Kamiński, T., Wong, K. T., Schmidt, M. R., et al. 2016, A&A, 592, A42
Kervella, P., Montargès, M., Ridgway, S. T., et al. 2014, A&A, 564, A88
Khouri, T., Maercker, M., Waters, L. B. F. M., et al. 2016, A&A, 591, A70
Kumar, S. S., Hauser, D., Jindra, R., et al. 2013, ApJ, 776, 25
Leão, I. C., de Laverny, P., Mékarnia, D., de Medeiros, J. R., & Vandame, B. 2006, A&A, 455, 187
Lindqvist, M., Nyman, L.-A., Olofsson, H., & Winnberg, A. 1988, A&A, 205, L15
Lombaert, R., Decin, L., Royer, P., et al. 2016, A&A, 588, A124
Mauron, N., & Huggins, P. J. 2000, A&A, 359, 707
Mauron, N., & Huggins, P. J. 2006, A&A, 452, 257
McElroy, D., Walsh, C., Markwick, A. J., et al. 2013, A&A, 550, A36
Millar, T. J., Walsh, C., Cordiner, M. A., Ní Chuimín, R., & Herbst, E. 2007, ApJL, 662, L87
Montez, R., Jr., Ramstedt, S., Kastner, J. H., Vlemmings, W., & Sanchez, E. 2017, ApJ, 841, 33
Neufeld, D. A., González-Alfonso, E., Melnick, G. J., et al. 2011, ApJL, 727, L28
Ortiz, R., Guerrero, M. A., & Costa, R. D. D. 2019, MNRAS, 482, 4697
Quintana-Lacaci, G., Cernicharo, J., Agúndez, M., et al. 2016, ApJ, 818, 192
Quintana-Lacaci, G., Cernicharo, J., Velilla Prieto, L., et al. 2017, A&A, 607, L5
Ramstedt, S., Mohamed, S., Vlemmings, W. H. T., et al. 2017, A&A, 605, A126
Saberi, M., Vlemmings, W. H. T., De Beck, E., Montez, R., & Ramstedt, S. 2018, A&A, 612, L11
Sahai, R., Findeisen, K., Gil de Paz, A., & Sánchez Contreras, C. 2008, ApJ, 689, 1274
Sahai, R., Neill, J. D., Gil de Paz, A., & Sánchez Contreras, C. 2011, ApJL, 740, L39
Sahai, R., Sánchez Contreras, C., Mangan, A. S., et al. 2018, ApJ, 860, 105
Schmidt, M. R., He, J. H., Szczerba, R., et al. 2016, A&A, 592, A131
Senent, M. L., & Hochlaf, M. 2013, ApJ, 768, 59
Van de Sande, M., Decin, L., Lombaert, R., et al. 2018a, A&A, 609, A63
Van de Sande, M., Sundqvist, J. O., Millar, T. J., et al. 2018b, A&A, 616, A106
Wittkowski, M., Hofmann, K.-H., Höfner, S., et al. 2017, A&A, 601, A3
Yen, T. A., Garand, E., Shreve, A. T., & Neumark, D. M. 2010, JPCA, 114, 3215